On Predicting In-building WiFi Coverage with a Fast Discrete Approach

G. de la Roche*, K. Jaffrès-Runser and J.-M. Gorce
ARES, INRIA,
CITI, INSA-Lyon (National Institute of Applied Sciences),
F-69621, France
E-mail: guillaume.de-la-roche@insa-lyon.fr
* corresponding author

Abstract: A new approach for predicting coverage of wireless LAN at $2.4GHz$ is presented. Coverage prediction is one of the core parts of indoor wireless LAN planning tools. The main concern it has to deal with is providing a good trade-off between prediction accuracy and computational load. Usual approaches belong to either empirical or deterministic methods. A new perspective has recently been offered that exploits a discrete formalism based on the TLM formulation. It is referred to as MR-FDPF (Multi-Resolution Frequency Domain ParFlow). While ray-tracing handles computational load by restricting the number of considered paths, the proposed approach acts by adapting the spatial resolution. This paper presents the straight lines of MR-FDPF and details the conditions for efficient in-building coverage prediction at $2.4GHz$. In a second part the paper tackles the calibration problem and claims for an automatic calibration process to improve the fit between predictions and measurements. A couple of experiments are presented.

Keywords: Indoor propagation, TLM, ParFlow, WLAN planning, coverage predictions.

Reference to this paper should be made as follows: de la Roche, G., Jaffrès-Runser, K. and Gorce, J.-M. (2007) 'On Predicting In-building WiFi Coverage with a Fast Discrete Approach', Int. J. High Performance Computing and Networking, Vol. X, Nos. y, pp.00–00.

Biographical notes: Guillaume de la Roche graduated in telecommunication engineering in 2003 from CPE Lyon and received the MSc. degree from INSA Lyon . He is currently a PhD student in the CITI laboratory of INSA Lyon, under the supervision of Dr. Jean-Marie Gorce.
Katia Jaffrès-Runser received her MSc. (2002) and PhD. (2005) from the INSA university in Lyon , France. In 2006, she joined the Stevens Institute of Technology in Hoboken, NJ, USA as a post-doctoral researcher where she's working with Pr. Comaniciu on wireless ad hoc and sensor networks optimization. She received a 3-year Marie-Curie fellowship from EU to pursue her work in 2007 in both Stevens I.T. and INSA Lyon.
Jean-Marie Gorce received the Dipl. Ing. (M.Sc.) degree in electrical engineering from the National Institute of Applied Sciences (INSA), Lyon, France, in 1993. He completed his PhD thesis in 1998. He joined the telecommunications department at INSA Lyon as an associate professor in 1999. He is head of the radio modelling axis of CITI Laboratory.

1 INTRODUCTION

WiFi and other new wireless technologies for LANs are spreading out everywhere, from private houses, corporate buildings to public areas, in both indoor and outdoor environments. To face the mostly uncontrolled development of multiple systems sharing the same ISM band, many efforts are devoted to optimizing the deployment of interfering networks (Sherali et al., 1996; Aguado Agelet et al., 2002; Unbehaun and Kamenetky, 2003; He et al., 2004; Amaldi

et al., 2005; Bahri and Chamberland, 2005; Jaffrès-Runser et al., 2006). Such a task relies on simulation tools having the ability of predicting the behavior of solutions before deployment. Such tools need accurate but fast coverage predictions. Even if research has been performed in this area for over fifteen years, simulation of radio wave propagation is still a hard task for highly complex indoor environments. Now the main concern is to get a competitive trade-off between computational load and accuracy where small processing times does not affect too much the prediction quality. New applications are also longing for efficient coverage prediction like *ad hoc*, sensor networks (Zhou et al., 2006) or MIMO systems simulations (Oh and Myung, 2004).

As for micro-cell planning in urban areas, there are two kinds of propagation modellings that are widely used for indoor pico-cells: empirical and deterministic approaches (COST 231, 1996; Neskovic et al., 2000). Indoor environments however strongly differ from urban ones: although dealing with smaller areas, the propagation is more complex because of the existence of much more reflection and diffraction effects on each path. It is one of the main reasons why empirical models struggle to provide accurate results. Thus, the simplest one-slope model (1SM) was enhanced in COST 231 (1996) and also by (Cheung et al., 1998) who proposed the multi-wall model (MWM). MWM takes wall effects along the direct path into account but neglects multiple lateral paths. Hassan-Ali and Pahlavan (2002) proposed an enhanced empirical approach accounting for statistically distributed multi-path in an ellipsoid located around the main path.

Many works have been developed under the UTD formalism since the beginning of the nineties, providing many variations around ray-tracing (McKnown and Hamilton, 1991; Honcharenko et al., 1993; Seidel et al., 1993). The large bulk of recent papers focused either on improving the accuracy (Suzuki and Mohan, 2000; Athanasiadou and Nix, 2000b,a) or on reducing the computational complexity (Wolfle et al., 2004; Aguado Agelet et al., 2000; Imai and Fujii, 2002; Ji et al., 2001; Chen et al., 2004). These approaches converge to really accurate solutions when a high number of rays are launched. Although very attractive these methods are strongly affected by the trade-off between computational load and accuracy. Indeed, accuracy calls for a fine angular sampling and the management of numerous reflections, while both are widely time-consuming. Suzuki and Mohan (2000) overcome the first shortcoming by introducing the beam-tracing technique. Reducing the computational load is often achieved by limiting reflections or diffractions. This may not be appropriate for indoor prediction due to peculiar effects such as wave guiding in corridors. Wolfle et al. (2004) faced the computational load issue by introducing the concept of the dominant path model (DPM). DPM is firstly based on a visibility graph calculus to avoid the highly time consuming search of rays and walls intersections, as also proposed by Suzuki and Mohan (2000). DPM is then derived by removing all paths except the one providing the most part of power, i.e. the dominant path. It should be noticed however that the dominant path does not correspond to a unique physical path but rather to a combination of main multi-paths. Hence, the still high computational load of propagation prediction is the main limit for the efficient use of simulation tools in common engineering tasks. This is due to the fact that a planning process requires hundreds or even thousands of coverage estimations.

In this framework, the use of a discrete based method may appear senseless at first sight. This may be why only few works tackled this problem with exact finite element approaches Zygiridis et al. (2006); Lee and Lai (1998); Talbi (1996). ParFlow introduced by Chopard et al. (1997) is probably the only one that efficiently implements a discrete method for cellular network planning. More recently ParFlow has been proposed for indoor propagation prediction by Gorce et al. (2003) using a frequency domain formulation. Assuming that the single harmonic response is significant, this formulation lead to a linear inverse problem. Its exact resolution was performed by an algorithm called MR-FDPF (Multi-Resolution Frequency Domain ParFlow) fully detailed in Gorce et al. (2005, 2007). Implementing this algorithm in the $2.4GHz$ band is the scope of this paper. It is shown that a drastic reduction of the computational complexity is achieved using reasonable approximations.

The second focus of this paper concerns the calibration process. For lots of roll-out situations, it is not possible to have the complete knowledge of the environment (wall's material, precise dimensions, furniture, ...). This concern matters for any propagation method. The calibration process herein proposed allows the designer for introducing a bit of realism in the simulations and to further compensate for the approximations associated with the prediction method.

2 MR-FDPF THEORY

This section gives a general outline of the $2D$ Frequency-Domain ParFlow (FDPF) method. The reader is referred to Gorce et al. (2005, 2007) for a complete description. Although the ParFlow theory and its frequency domain formulation is proposed by de la Roche and Gorce (2006) in three dimensions, this paper focuses only on the $2D$ implementation for the purpose of computational efficiency. A $2,5D$ extension is detailed in section 3.

2.1 The frequency domain ParFlow (FDPF)

Like other finite difference approaches, ParFlow (Partial Flows) is based on the Maxwell's equations. In two dimensions (2D), the electrical field $\Psi(\mathbf{r}, t)$ is assumed scalar (i.e. vertical TE). When compared to other FDTD approaches, ParFlow, as TLM, gets its originality from the fact that the electrical field is divided into 4 directive flows (see Fig.1a), each one carrying energy to a cardinal direction (Gorce et al., 2005). These flows are driven by a local transition

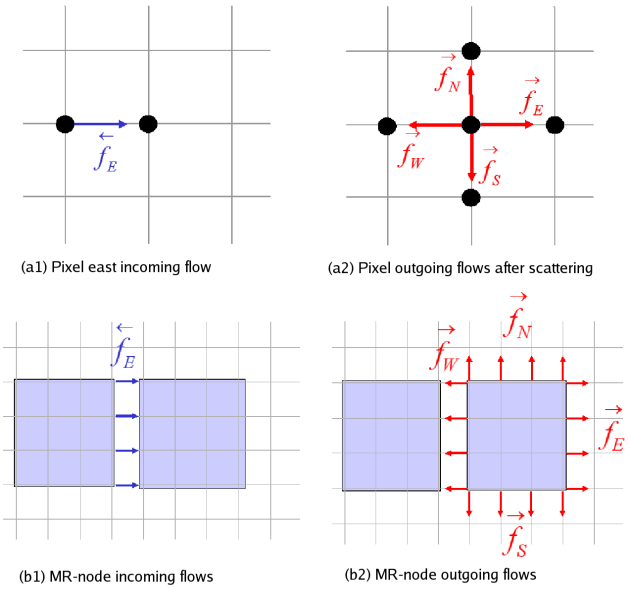

Figure 1: The TLM principle is illustrated at the pixel level (a) and at a block level (b). The east incoming flow from west neighbor is scattered in the 4 directions according to the scattering matrix.

matrix derived from the discrete Maxwell's wave equations and are referred to as $\overleftarrow{f_d}$ and $\overrightarrow{f_d}$ respectively for inward and outward flows. The index $d, (d \in \{E, W, S, N\})$ indicates the flow's direction (East, West, South, North). In the frequency domain (FD) steady-state neighbor flows are bound by the FD scattering equation

$$\overrightarrow{F}(m) = \Sigma_f(m) \cdot \overleftarrow{F}(m) + \overrightarrow{S}(m) \tag{1}$$

$\overleftarrow{F}(m)$, $\overrightarrow{F}(m)$ and $\overrightarrow{S}(m)$ are respectively inward, outward and source vectors according to
$F = (\ f_E \quad f_W \quad f_S \quad f_N\ )^t$.
$\Sigma_f(m)$ is the local scattering matrix at pixel $m : \{i, j\}$ and frequency f, having its own coefficients according to the material (air, concrete, ...) located in m. Gathering all flows into a unique vector $\underline{\overrightarrow{F}}$ leads to a linear inverse problem:

$$(I_d - \underline{\Omega}) \cdot \underline{\overrightarrow{F}} = \underline{\overrightarrow{S}} \tag{2}$$

where $\underline{\Omega}$ is a wide sparse penta-diagonal matrix that gathers all the relations between the nodes of the environment. The main concern is to determine completely $\underline{\overrightarrow{F}}$.

2.2 MR-node definition

The MR-node is the first element of the MR-FDPF approach. A MR-node (multi-resolution node) b_k refers to a rectangular set of pixels. For each MR-node b_k, inward and outward *exchange* flow vectors resp. $\overleftarrow{F_e}(b_k)$ and $\overrightarrow{F_e}(b_k)$ are associated with each side, according to Fig.1b. Compared to the usual ParFlow scattering matrix, the only difference relies on the vectorial nature of the flows. They are still bound by a local scattering equation:

$$\overrightarrow{F_e}(b_k) = \Sigma_e(b_k) \cdot \overleftarrow{F_e}(b_k) + \overrightarrow{S}_e(b_k) \tag{3}$$

2.3 Multi-resolution tree

Secondly, the MR-FDPF algorithm relies on the definition of a multi-resolution binary tree binding conventional TLM nodes (i.e. unitary MR-nodes) into a unique head node as depicted in Fig.2. The tree is built in a recursive way starting from the head node: each MR-node is divided along its main discontinuity line (i.e. along a wall), providing two child MR-nodes. The division along each branch of the tree is firstly stopped when a homogeneous MR-node is reached. A MR-node is said homogeneous if it contains a single material as for instance air or concrete. Each homogeneous MR-node is then itself split into children nodes along the median line. This process is repeated for its children nodes, until unitary nodes i.e. pixels size nodes are obtained.

2.4 Computing the scattering matrices

To exploit the binary tree, relationships between the flows of father and child MR-nodes are needed. For the sake of clarity, let be considered the case of a node b_k having two child nodes b_i and b_j gathered horizontally (b_i on the left hand side and b_j on the right hand side). Children's flows bringing energy from one child to the other (i.e.$\overrightarrow{f_E}(b_i)$ and $\overrightarrow{f_W}(b_j)$) are referred to as the father node's inner flows:

$$f_0(b_k) = \begin{pmatrix} \overrightarrow{f_E}(b_i) \\ \overrightarrow{f_W}(b_j) \end{pmatrix} \tag{4}$$

The scattering matrix of b_k is obtained by computing the steady-state of inner flows as a function of inward flows. This calculus requires the knowledge of children's scattering matrices only. Then, starting from those of unitary MR-nodes, the scattering matrices of all MR-nodes in the binary tree are computed involving successive matrix inversions. Computation details are provided in Gorce et al. (2005). The overall complexity is evaluated in $O\left(N^3\right)$, for an environment of $N \times N$ pixels.

2.5 Coverage computation

2.5.1 Source propagation

The binary tree is then used to compute the field generated by a point source located anywhere in the building, in two successive steps: the bottom-up computation of equivalent sources and the top-down computation of inward flows.

- *The bottom-up phase* starts at the elementary source node. Outward flows of its father node are firstly computed changing the father node into a new source MR-node. This process is repeated until the outward flows

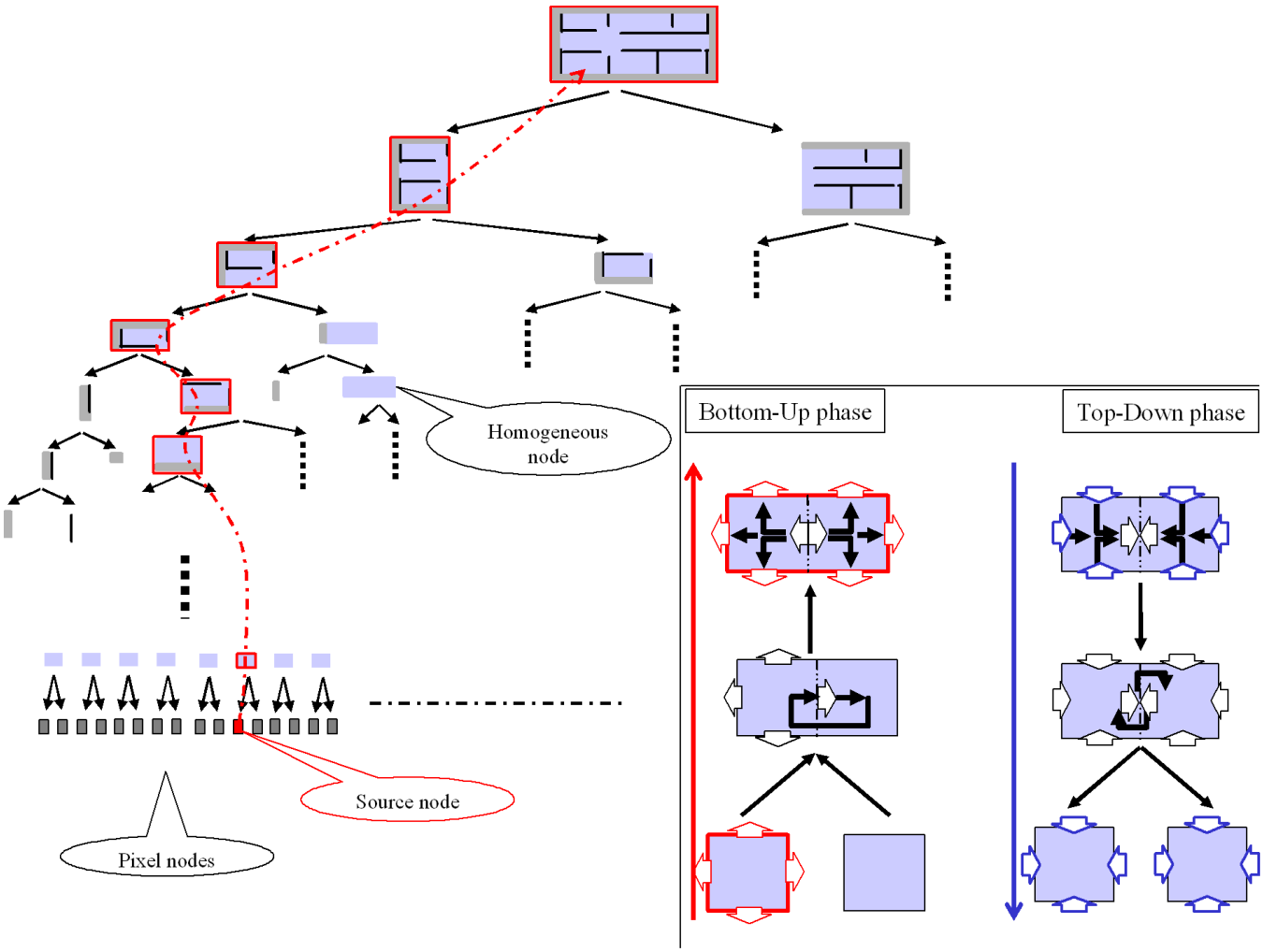

Figure 2: The binary tree is built starting from the head node (top). The division recursion acts on each node along the main discontinuity line. Terminal nodes are the usual ParFlow nodes (pixel nodes). The propagation of a source is computed in two phases: (i) The bottom-up phase exploits the sources' path in the tree and computes outward flows of equivalent sources. (ii) The top-down phase explores all branches and computes inner flows for each node.

of the head node are computed. All these nodes constitute the set of source MR-nodes. During this phase, inner source flows are stored (see Fig.2).

- *The top-down phase* starts by computing the steady-state inner flows for each MR-node from the values of their inward exchange flows and the previously stored inner source flows. Starting from the head node having null inward flows (boundary conditions), the computation is recursively done down to pixels nodes.

These calculus exploit the MR-nodes' scattering matrices and the complexity of the whole source propagation step is in $O\left(N^2 \cdot log(N)\right)$. This result outlines how the main computational load is really carried over to the preprocessing phase.

2.5.2 Mean field computation

The top-down propagation process can either stop at pixel nodes (all the pixel flows are computed) or more efficiently at any intermediate MR-node (preferably a homogeneous one) to directly compute the mean field from the inward flows according to :

$$P(b_k) = \frac{\|\overleftarrow{F}(b_k)\|^2}{2 \cdot (\Delta_x(b_k) + \Delta_y(b_k))} \tag{5}$$

where $\Delta_x(b_k)$ and $\Delta_y(b_k)$ denote the size of b_k. For coverage and mean receiving power predictions, such an averaging over large enough regions allows to compensate for fast fading. A spatially averaged power estimation appears being more robust than an exact field computation. A good trade-off is obtained when averaging is made over MR-nodes a bit larger than the simulation wavelength.

3 APPROXIMATIONS FOR INDOOR ROLL-OUT

3.1 Harmonic approximation

As the formalism is stated in the frequency domain, the study is limited to a harmonic mode and thus for a specific frequency. Such a harmonic steady-state study should be considered unappropriate because of time spreading and at a first glance, this points out a limit of the MR-FDPF model. However, the full channel impulse response can be easily assessed by processing coverage predictions for several frequencies around the carrier. Time spreading issue is kept out of the scope of this paper, focusing on mean power coverage prediction. This choice is argued by the fact that the time spreading of the radio channel in indoor environments at $2.4GHz$ (or $5GHz$) is small compared to the symbol duration in WiFi frames.

3.2 Radiation pattern synthesis

Although omnidirectional antennas like dipoles or whips are widely used for APs, directional antennas are sometimes preferred to increase the AP's range. Including a radiation pattern in ray-tracers is easier than in the FDPF approach where point sources are essentially omnidirectional. This issue can be overcome by radiation pattern synthesis exploiting arrays of point sources, in both receiving and transmitting modes. This approach is detailed in Villemaud et al. (2006).

3.3 $2D$ approximations

The MR-FDPF algorithm is herein studied in $2D$ only because the $3D$ derivation exhibits a strong computational load. The first fundamental limit of the $2D$ modelling holds in the fact that the natural $2D$ free-space pathloss increases in $PL(r) = r^n$ having $n = 1$ instead of $n = 2$ for $3D$. It is worth noting however that in a confined environment, the ceiling and the floor act as a waveguide where multiple reflections lead to $n < 2$. To compensate for the possible inaccuracy of the 2D modelling, an attenuation coefficient α_{air} is introduced in the propagation matrix of air-made pixels, modifying the pathloss model according to:

$$PL(r) = r \cdot exp(\alpha \cdot r) \tag{6}$$

This model fits the $3D$ free-space model, in a finite range of at least one decade, with an error lower than $2dB$, as illustrated in Fig.3.

To estimate the coverage of multi-floored buildings, an *ad hoc* extension of the $2D$ algorithm is proposed. For the sake of clarity, let be considered the simplest case of an AP located on floor n while the coverage is estimated on floor $n + 1$.

- **Direct Field Projection:** the simplest approach firstly computes the coverage at the source floor n, only accounting for the obstacles of floor n. The coverage at the $n + 1$ floor is then directly inferred by applying a mean attenuation factor representative of the ceiling attenuation.

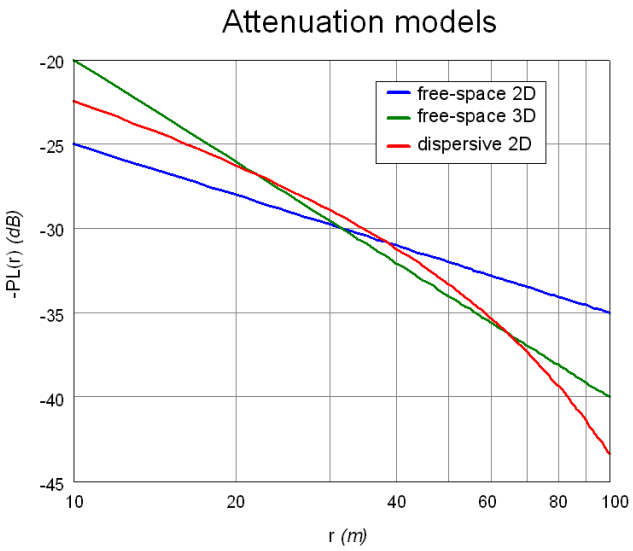

Figure 3: Example of attenuation models. The dispersive model is obtained thanks to the additive attenuation coefficient chosen to fit the 3D free-space model with a 2D modelling. Note that a different scaling factor is used for each model. The meaning of the scaling factor is discussed in next section.

- **Equivalent Source:** Another simple approach is to compute an equivalent attenuated source at floor $n+1$. The virtual source is propagated in its own floor and does not further depend on floor n arrangement.

- **Combined Source-Field:** Because both previous approaches cannot deal simultaneously with the geometry of both floors, a combined approach seems attractive. The propagation is firstly computed at the transmitter's floor. All flows are then stored and used as source flows at the receiver floor, after applying a ceiling attenuation factor. Thus, all pixel's flows computed at level n, act as source flows at level $n+1$ after proper weighting. All of these source flows are propagated at the receiver floor, leading to a new coverage map.

At first glance the combined approach could appear time-consuming since each pixel is considered as a source at the receiver floor. Nevertheless, an efficient implementation is used: the bottom-up phase of the MR-FDPF algorithm can propagate simultaneously all sources, while keeping unchanged the top-down phase. The overall complexity is therefore only twice as much as the one of the initial method.

3.4 Simulation frequency and spatial resolution

In discrete approaches, the spatial resolution Δ_R is constrained by the wavelength. Luthi (1998) suggests the empirical limit $\Delta_R \leq \lambda_s/6$ to prevent from anisotropy errors.

The resolution step Δ_R should thus be lower than $2cm$ at $2.4GHz$ (i.e. for $802.11b/g$). Such a resolution appears very low when compared to the resolution at which coverage values are reasonably expected: a prediction returning one value for each square meter seems reasonable. Furthermore, working at such a resolution is unrealistic as exact position of walls, furniture and people is not known with such a level of details. Because the computational load heavily depends on the environment size, WLAN planning would benefit from a better trade-off between computational load and accuracy. The simulation frequency is thus chosen lower than the operational frequency.

Only few mismatch effects ensue. First of all, the inherent free-space path-loss shift is easily compensated for by the use of an appropriate calibration constant (see next section). Secondly, walls' reflection and transmission coefficients, usually depending on the frequency, can be set according to the actual frequency.

A first uncompensated discrepancy follows from diffraction at corners: rays are not exactly positioned. We believe however that in terms of amplitude, the mismatch remains marginal. Last but not least, the main effect of changing the frequency rests on flat fading due to multipath (after both reflection and diffraction) occurring everywhere in indoor. Indeed, phase combination in multipath environment is very sensible to the simulation frequency, and leads to matchless fading patterns. However, it is claimed that a mean power prediction remains significant after a spatial averaging. Thus, a mean field estimation over large enough MR-nodes is used.

The simulation frequency is finally chosen as a trade-off between realism (short wavelength) and computational load. To permit a robust mean field estimation for MR-nodes of $1m^2$ surface area, the wavelength has to be lower than $1m$. In the following, the reference simulation parameters are set to

$$\Delta_R = 10cm \quad \text{and} \quad \nu_s = 480MHz \tag{7}$$

while the real frequency is of $2.4GHz$. Notice that the simulation wavelength has been chosen as a multiple of the operational wavelength to reduce the discrepancy due to diffraction.

4 CALIBRATION PROCESS

Whatever the modelling approach is, binding simulations to real values is always a delicate problem due to the lack of exact conditions knowledge: exact antenna gain, radiation pattern, transmission power, material properties, furniture, etc. In this work a blind approach is proposed exploiting a calibration process based on a set of measurements.

4.1 Calibration offset

Real field predictions Ψ_{pred} are obtained from simulated values Ψ_s thanks to a calibration offset C_Ψ:

$$\Psi_{pred}(dBm) = \Psi_s(dB) + C_\Psi(dBm) \tag{8}$$

The numerical source could here be bound formally to an ideal current source Gorce et al. (2005). This relationship is however corrupted by previously stated approximations making senseless any formal calibration offset determination.

This process requires as input a set of experimental measurements. The calibration offset is chosen to minimize the root mean square error (RMSE) between M experimental values $\Psi_{mes}(i),\ i \in [1..M]$ and corresponding predictions, leading to the following optimal calibration offset

$$\tilde{C_\Psi} = \frac{1}{M}\sum_{i=1}^{M}\left(\Psi_{mes}(i) - \Psi_s(i)\right) \tag{9}$$

providing a null mean error $e(i) = \Psi_{mes}(i) - \Psi_{pred}(i) = 0$. The adequacy of the calibrated prediction model can be assessed thanks to the resulting RMSE, itself equal to the variance: $\langle \tilde{e}(i)^2 \rangle = \sigma_e^2$.

4.2 Material parameters n and α

As previously mentioned, the free-space attenuation coefficient has to be determined. Each material in ParFlow is defined by two parameter: the refraction index n and the electrical permittivity on which the attenuation coefficient α relies. Both are used in the scattering matrix of TLM nodes. Although experimental values can be found in literature, their dependency to the actual composition of materials makes a default setting senseless. That is why the couples (n, α) associated with each material are relaxed too. These parameters constitute the set of unknowns associated with a peculiar environment referred to as $\omega \in \Omega$. The optimal set of parameters and the calibration offset are jointly estimated according to

$$\begin{aligned} \tilde{C_\Psi}(\omega) &= \frac{1}{M}\sum_{i=1}^{M}\left(\Psi_{mes}(i) - \Psi_s(i/\omega)\right) \\ \tilde{\omega} &= \arg\min_{\omega\in\Omega}\left(\sigma_e^2(\tilde{C_\Psi}(\omega), \omega)\right) \end{aligned} \tag{10}$$

Thus, $\tilde{C_\Psi}$ sets the mean error to zero while $\tilde{\omega}$ minimizes the standard deviation.

4.3 Minimization algorithm

The resulting minimization problem is a hard optimization problem. Firstly, the problem is not convex and presents several local minima. Secondly, the computational load to evaluate one set of parameters is high as the preprocessing stage of MR-FDPF has to be run for each set independently. Since an exhaustive search of all possible settings is not affordable, a heuristic approach adapted to this problem is proposed. Because the search space is continuous

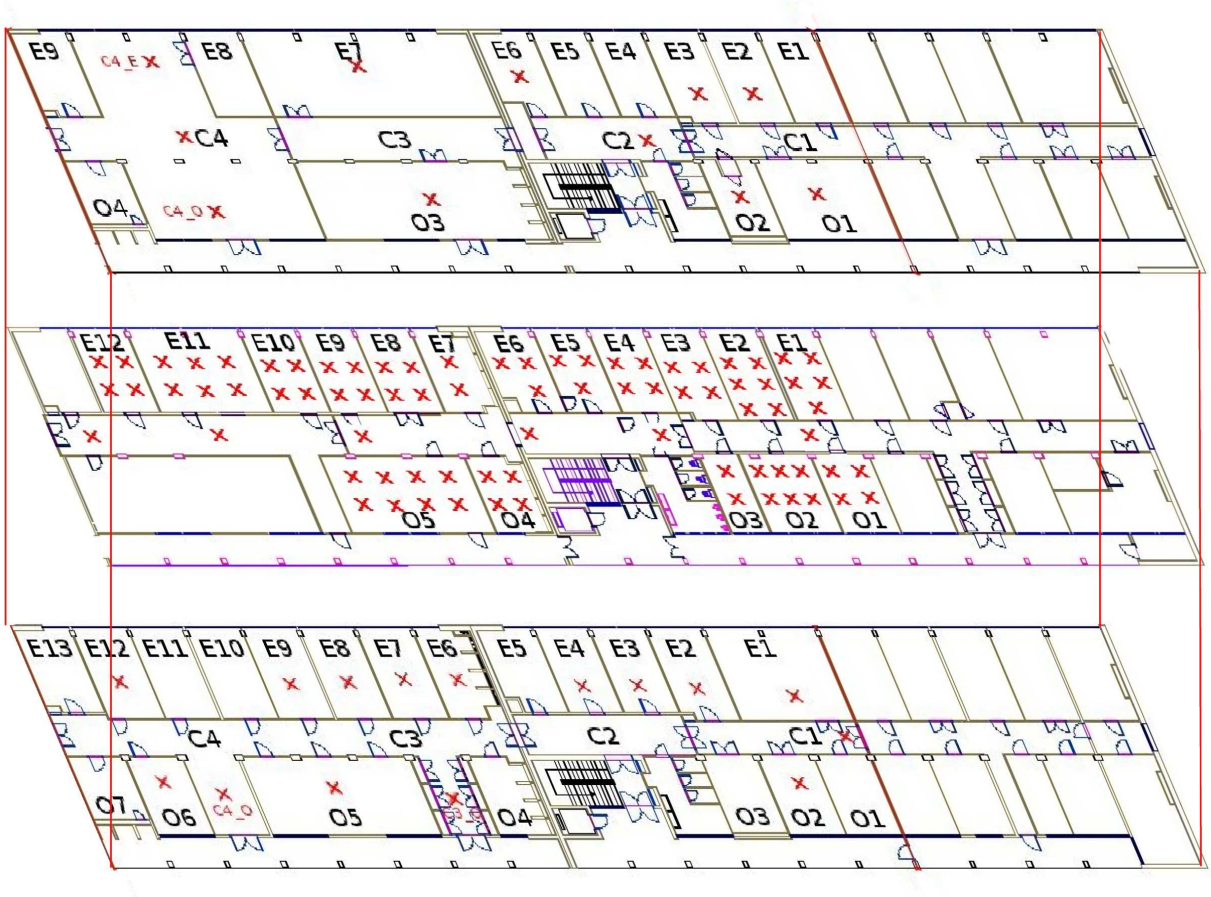

Figure 4: Experimental configuration. The test building is made of three floors. The source is located in room $E7$ at intermediate level. Measurement points are indicated by red crosses.

and the derivatives of the cost function can not be analytically assessed, gradient based methods are excluded and the direct search algorithm proposed by Jones et al. (1993) is chosen. This method alternates global and local search and aims at realizing an exhaustive search at infinity. The process stops when an acceptable solution is reached.

4.4 Efficiency evaluation

Of course, the results may heavily rely on the quality and the representativeness of the measurements. The optimal solution is optimal only for the environment under test and for the configuration used for calibration. It is in fact more robust to use measurements from numerous regularly spaced locations and for several APs. Note that the calibration computational load associated to the simulations does not depend on the number of test points and APs as preprocessing represents the main load.

The quality of the final solution can be assessed by answering these three questions:

- What is the efficiency of the predictions for the present test set? The answer is provided by the final error variance.
- Is the calibration efficient for other APs' locations in the same environment? The answer is obtained by performing calibration for several experimental subsets. This question is crucial for the use of the predictions in a WLAN planning tool.
- Is the calibration efficient for other environments? The answer is based on the predictions' accuracy estimation for several test environments. The answer allows to know if calibration results are portable.

5 RESULTS

5.1 Harmonic mode

5.1.1 VSA base measurements

The method has been firstly assessed with calibrated radio measurements in harmonic mode. The measurement platform consisted of an arbitrary waveform generator (ESG4438C of Agilent Technology ©) and a vector signal analyzer (VSA 89641 of Agilent Technology ©), both equipped with $2.4GHz$, $4dBi$, omnidirectional antennas. A pure sinusoïdal waveform was generated and the span

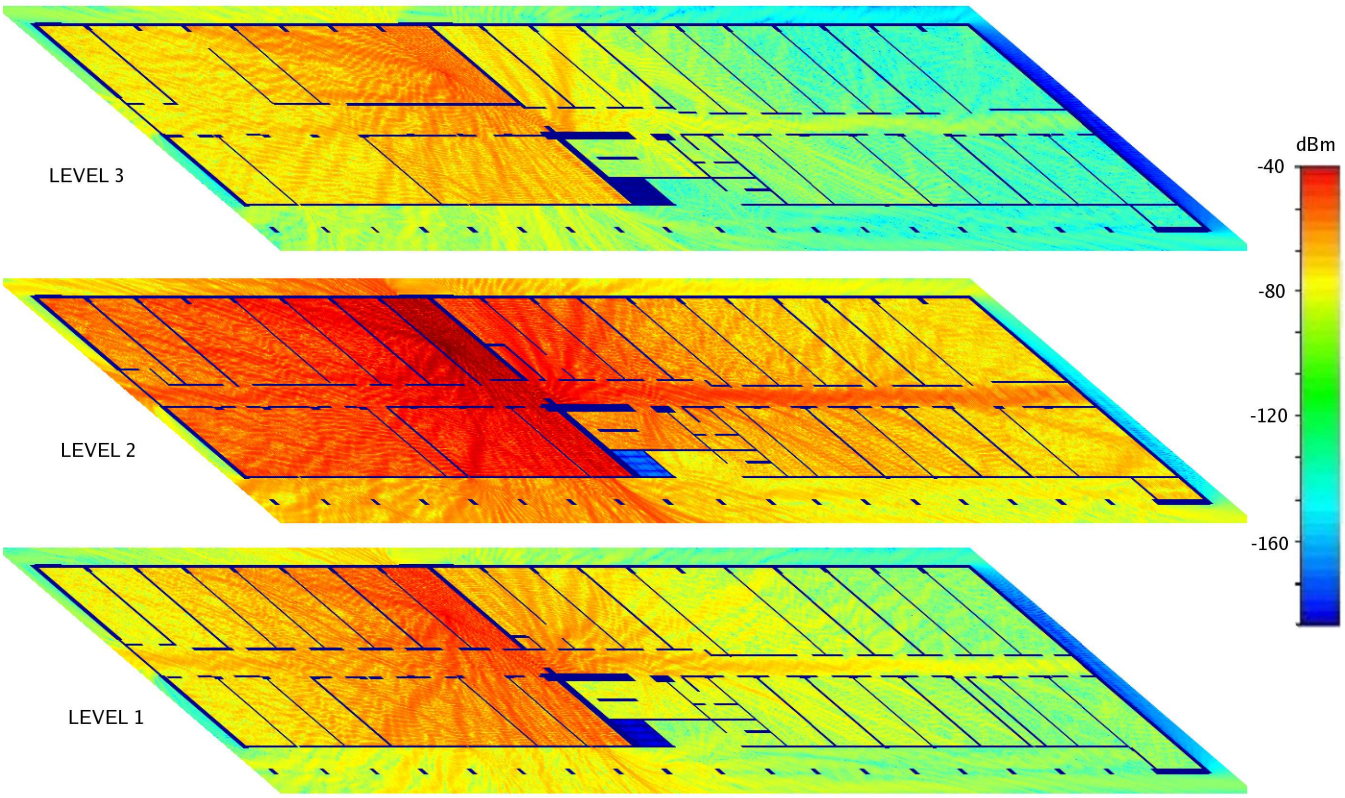

Figure 5: Coverage areas at each floor of the building

of the receiver was fixed at $2kHz$ allowing measurements from $-40dBm$ down to $-110dBm$. For each referred position (*cf.* red crosses on Fig.4), about 200 measurement samples were collected during $60s$ with slow displacements and rotations to obtain a mean value compensated for flat fading. The source was located at floor 2, in room E7. Measurements were taken at 80 locations at the source floor and respectively at 11 and 15 locations for the upper and lower floors.

5.1.2 Calibration

Each floor is made of three different types of walls:

- concrete walls for the main load-bearing walls.
- plaster walls corresponding to standard walls between rooms.
- glazed walls corresponding to the external walls made of windows.

So 3 couples (n, α) are optimized during the calibration process. The previously described calibration algorithm is used at 4 resolution steps ($5cm$, $10cm$, $20cm$ and $50cm$) with respectively the following simulation frequencies: $960MHz$, $480MHz$, $240MHz$ and $96MHz$. Calibration results show that the attenuation coefficient of walls has a low impact on the simulations. This result can be assigned to the thin thickness of walls in comparison to the simulation wavelength. On the contrary, the air attenuation factor impacts strongly the predictions because it modifies the attenuation law. However, the best predictions are obtained with $\alpha_{air} = 1.0$. This corresponds to a logarithmic attenuation slope proportional to d^{-1}, corresponding to a 2D free-space propagation model. This can be charged to the fact that the transmitter was situated in a regular multi-floor building in which waves are bounded by the floor and the ceiling.

After calibration, we found the following values for parameter n: 5.4 for concrete walls, 2.4 for plaster walls and 1.3 for glazed walls. Only slight variations are observed as a function of the resolution step. These values are eventually close to experimental values provided in the literature.

5.1.3 Results

The theoretical computational load relies on the resolution step as we have $O\left(dr^{-3}\right)$ and $O\left(dr^{-2}\right)$ for preprocessing and propagation phase respectively. Experimental results are summarized in table 1. While computational load behaves according to theory, the RMSE appears roughly constant for a resolution step lower than $20cm$.

The RMSE increases rapidly for a resolution higher than $20cm$. Coverage areas at $5cm$ are shown in Fig.5. Simulation and measurements for the previously described points are compared on Fig.6. On this figure most of the measurement points are located between two dotted lines bounding the area where the error between prediction and measure-

Table 1: Computational time achieved on a Pentium IV, 2.4GHz, with 3Gb RAM

step size	*RMSE*	*preprocess*	*block propag*	*pixel propag*
5cm	3.88dB	53 s	0.8 s	6.5 s
10cm	4.07dB	8 s	0.2 s	1.6 s
20cm	4.06dB	2 s	0.08 s	0.4 s
50cm	7.2dB	0.05 ms	0.04 s	0.06 s

ment is less than 5dB.

5.2 WiFi coverage predictions

5.2.1 Experimental setup

Harmonic measurements don't rely exactly on the real WiFi power reception level due the lack of knowledge on reception equipments (sensitivity, gain, ...) and antennas radiation patterns. To evaluate the suitability of this approach for WiFi planning, complementary WiFi coverage predictions have been assessed by three measurement campaigns done in two buildings. For each measurement location, about 300 samples were recorded during $60s$ with an 802.11b PCMCIA Orinoco© receiver nested in a laptop. During the recording time, slow displacements and rotations have been performed to get a mean value compensated for flat fading as done for harmonic measurements. A local mean power and a standard deviation have been calculated for each point. The three measurements sets are the following:

1. $CITI_1$ set: 199 measurement locations recorded in the intermediate floor of Fig.4. Six different APs have been deployed for this purpose.
2. $CITI_2$ set: 15 measurement points located on the same floor covered by 3 other APs.
3. *BuildingG* set: 15 measurement points located in another building covered by one access point.

For each data set, the same previously defined materials were assumed: concrete, plaster and glazed wall. Calibration of the simulator with $CITI_1$ provided roughly the same values for (n, α) than the harmonic study.

$CITI_2$ and *BuildingG* were used to calculate the accuracy of the simulations after calibration with $CITI_1$.

5.2.2 Calibration performance

The calibration of the 3 indices based on the $CITI_1$ data set needed roughly 1800 function evaluations to converge. The more parameters DIRECT had to find out, the more evaluations were processed. As one evaluation can last up to 1 minute depending on the environment size, it is sensible to validate the portability of the indices found. If indices can be re-used, a single calibration offset can be computed based on a couple of measurements to simply annihilate the mean prediction error $\langle \tilde{e}(i) \rangle$.

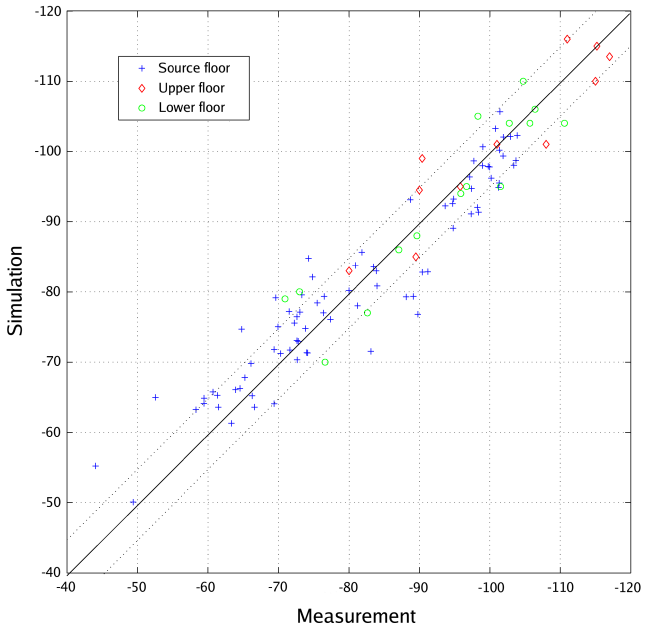

Figure 6: Comparison between predictions and harmonic measurements

5.2.3 Error analysis

Validation of the calibration offset $\tilde{C_\Psi}$ and the indices has been done by computing the RMSE $\langle \tilde{e}(i)^2 \rangle$, the mean error $\langle \tilde{e}(i) \rangle$ and the standard deviation σ_e^2 of the prediction errors occurring when comparing predictions and measurements of $CITI_2$ and *BuildingG* data sets. For $CITI_2$, an RMSE of $5.1dB$ has been obtained with a mean error of $\langle \tilde{e}(i) \rangle = -2dB$ and a standard deviation of $\sigma_e^2 = 4.65dB$. For *BuildingG*, an RMSE of $5.0dB$ has been obtained with a mean error of $\langle \tilde{e}(i) \rangle = -2dB$ and a standard deviation of $\sigma_e^2 = 4.3dB$. The fit between simulations and measurements for the $CITI_2$ set assesses stability of the predictions in the same building. The results of *BuildingG* assess the portability of the predictions to another similar environment.

The RMSE values are similar to those obtained with $CITI_1$ while the mean error is of about -2dB for both validation sets. This mean error can easily be removed by a simple calibration offset adjustment. Based on those results, we can claim that calibrated MR-FDPF predictions are truly efficient for WiFi planning.

6 CONCLUSIONS

Indoor propagation prediction is an important issue in the development of wireless technologies. The proposed discrete approach offers an original way to produce fast multi-

path predictions. The fundamental trade-off between complexity and coarseness is herein managed by the selection of the simulation frequency rather than the number of simulated paths as done with ray-tracing based approaches. Mean power predictions may be used in many contexts, including WLAN planning, indoor mobile equipment positioning or interference management. The simulator also opens for a promising way of simulating and evaluating *ad hoc* and sensor networks in an indoor context. The multi-resolution algorithm is indeed truly adapted to simulating mobile multi-nodes networks: thanks to the preprocessing phase, computing peer to peer radio links is very fast.

In future works, the simulations could be significantly improved by relaxing the computational load constraint. i) The true frequency could be used. ii) The local impulse response could be built by running the simulator at several frequencies around the carrier. iii) Full 3D simulations could be performed. Such a framework appears promising for simulating indoor radio networks, including a realistic channel model. Furthermore, the simulator may easily include multiple antenna simulations for the evaluation of MIMO systems such as expected, for instance, for future 802.11n compliant systems.

REFERENCES

Aguado Agelet, F., Formella, A., Hernando Rabanos, J., Isasi de Vicente, F., and Perez Fontan, F. (2000). Efficient ray-tracing acceleration techniques for radio propagation modeling. *IEEE Trans. on Vehicular Technology*, 49(6):2089–2104.

Aguado Agelet, F., Varela, A., Alvarez-Vazquez, L., J.M., H., and Formella, A. (2002). Optimization methods for optimal transmitter locations in a mobile wireless system. *IEEE Trans. on Vehicular Technology*, 51(6):1316–1321.

Amaldi, E., Capone, A., Cesana, M., and Malucelli, F. (2005). Algorithms for WLAN Coverage Planning. *Lecture Notes in Computer Science*, 3427:52–65.

Athanasiadou, G. E. and Nix, A. R. (2000a). Investigation into the sensitivity of the power predictions of a microcellular ray tracing propagation model. *IEEE Trans. on Vehicular Technology*, 49(4):1140–1151.

Athanasiadou, G. E. and Nix, A. R. (2000b). A novel 3D indoor ray-tracing propagation model: The path generator and evaluation of narrow-band and wide-band predictions. *IEEE Trans. on Vehicular Technology*, 49(4):1152–1168.

Bahri, A. and Chamberland, S. (2005). On the wireless local area network design problem with performance guarantees. *Computer Networks*, 48(6):856–866.

Chen, Z., Bertoni, H. L., and Delis, A. (2004). Progressive and approximate techniques in ray-tracing-based radio wave propagation prediction models. *IEEE Trans. on Antennas and Propagation*, 52(1):240–251.

Cheung, K.-W., Sau, J. H.-M., and Murch, R. (1998). A new empirical model for indoor propagation prediction. *IEEE Trans. on Vehicular Technology*, 47(3):996–1001.

Chopard, B., Luthi, P., and Wagen, J. (1997). A lattice boltzmann method for wave propagation in urban microcells. In *IEE Proceedings - Microwaves, Antennas and Propagation*, volume 144, pages 251–255.

COST 231 (1996). *Digital Mobile Radio towards Future Generation Systems, Final Report*, chapter 4 : Propagation Prediction Models, pages 115–208. European Union, Brussels.

de la Roche, G. and Gorce, J.-M. (2006). Full 3D MR-FDPF method for the simulation of radio propagation. In *EUCAP*, Nice, France.

Gorce, J.-M., Jaffrès-Runser, K., and de la Roche, G. (2007). A deterministic approach for fast simulations of indoor radio wave propagation. *IEEE Trans. on Antennas and Propagation*, page in press.

Gorce, J.-M., Jullo, E., and Runser, K. (2003). An adaptive multi-resolution algorithm for 2D simulations of indoor propagation. In *Twelfth International Conference on Antennas and Propagation (ICAP)*, volume 1, pages 216–219, IEE, London, UK. Best Paper.

Gorce, J.-M., Runser, K., and de la Roche, G. (2005). The adaptive multi-resolution frequency-domain parflow (MR-FDPF) method for 2D indoor radio wave propagation simulation. part I : theory and algorithms. Research Report RR-5740, INRIA.

Hassan-Ali, M. and Pahlavan, K. (2002). A new statistical model for site-specific indoor radio propagation prediction based on geometric optics and geometric probability. *IEEE Trans. on Wireless Communications*, 1(1):112–124.

He, J., Verstack, A. A., Watson, L. T., Stinson, C. A., Ramakrishnan, N., Shaffer, C., Rappaport, T., Anderson, C. R., Bae, K. K., Jiang, J., and H., T. W. (2004). Globally optimal transmitter placement for indoor wireless communication systems. *IEEE Transactions on wireless communications*, 3(6):1906–1911.

Honcharenko, W., Bertoni, H., Dailing, L., Qian, J., and Yee, H. (1993). Mechanisms governing UHF propagation on single floors in modern office buildings. *IEEE transactions on Antennas and Propagation*, 41(6):787–790.

Imai, T. and Fujii, T. (2002). Fast algorithm for indoor microcell area prediction system using ray-tracing method. *Electronics and Communications in Japan, part 1*, 85(6):41–52.

Jaffrès-Runser, K., Gorce, J.-M., and Ubéda, S. (2006). QoS constrained wireless LAN optimization within a multiobjective framework. *IEEE Wireless Communications*, 13(6):in press.

Ji, Z., Li, B.-H., Wang, H.-X., Chen, H.-Y., and Sarkar, T. K. (2001). Efficient ray-tracing methods for propagation prediction for indoor wireless propagation. *IEEE Antennas and Propagation Magazine*, 43(2):41–49.

Jones, D. R., Perttunen, C., and Stuckman, B. (1993). Lipschitzian optimization without the lipschitz constant. *Journal of Optimization Theory and Applications*, 79(1):157–181.

Lee, J. W. H. and Lai, A. K. Y. (1998). FDTD analysis of indoor radio propagation. In *IEEE Antennas Propagation Society International Symposium*, volume 3, pages 1664–1667, Atlanta, GA.

Luthi, P. O. (1998). *Lattice Wave Automata : from radiowave to fracture propagation*. PhD thesis, University of Geneva, Geneva, Switzerland.

McKnown, J. W. and Hamilton, R. L. (1991). Ray tracing as design tool for radio networks. *IEEE Network Magazine*, 5:27–30.

Neskovic, A., Neskovic, N., and Paunovic, G. (2000). Modern approaches in modeling of mobile radio systems propagation environment. *IEEE communication surveys, http://www.comsoc.org/pubs/surveys*, pages 2–12.

Oh, S. and Myung, N. (2004). Mimo channel estimation method using ray-tracing propagation model. *Electronics letters*, 40(21):1350–1352.

Seidel, S. Y., Schaubach, K. R., Tran, T., and Rappaport, T. (1993). Research in site-specific propagation modeling for PCS system design. In *proc. 43rd IEEE Vehicular Technology Conference*, pages 261–264, Secaucus, NJ, USA.

Sherali, H. D., Pendyala, C. M., and Rappaport, T. S. (1996). Optimal location of transmitters for microcellular radio communication system design. *IEEE Journal on Selected Areas in Communications*, 14(4):662–673.

Suzuki, H. and Mohan, A. S. (2000). Measurement and prediction of high spatial resolution indoor radio channel characteristic map. *IEEE Trans. on Vehicular Technology*, 49(4):1321–1333.

Talbi, L. (1996). FDTD characterization of the indoor propagation. *Journal of electromagnetic waves and applications*, 10(2):243–247.

Unbehaun, M. and Kamenetky, M. (2003). On the deployment of picocellular wireless infrastructure. *IEEE Wireless Communications*, 10(6):70–80.

Villemaud, G., de la Roche, G., and Gorce, J.-M. (2006). Accuracy enhancement of a multi-resolution indoor propagation simulation tool by radiation pattern synthesis. In *I EEE Antennas and Propagation Society International Symposium*, pages 2153–2156, Albuquerque, New Mexico,USA.

Wolfle, G., Wahl, R., Wildbolz, P., and Wertz, P. (2004). Dominant path prediction model for indoor and urban scenarios. In *11th COST 273*, Germany.

Zhou, G., He, T., Krishnamurthy, S., and Stankovic, J. A. (2006). Models and solutions for radio irregularity in wireless sensor networks. *ACM Trans. on sensor networks 2006*, 2(2):221–262.

Zygiridis, T. T., Kosmidou, E. P., Prokopidis, K. P., Kantartzis, N. V., Antonopoulos, C. S., Petras, K. I., and Tsiboukis, T. D. (2006). Numerical modeling of an indoor wireless environment for the performance evaluation of WLAN systems. *IEEE Transactions on Magnetics*, 42(4):839–842.